NANO LETTERS

pubs.acs.org/NanoLett Letter

Controlled Formation of Stacked Si Quantum Dots in Vertical SiGe Nanowires

Emily M. Turner,* Quinn Campbell, Joaquín Pizarro, Hongbin Yang, Keshab R. Sapkota, Ping Lu, Andrew D. Baczewski, George T. Wang,* and Kevin S. Jones*

Cite This: *Nano Lett.* 2021, 21, 7905−7912 Read Online

ACCESS | Metrics & More | Article Recommendations | Supporting Information

ABSTRACT: We demonstrate the ability to fabricate vertically stacked Si quantum dots (QDs) within SiGe nanowires with QD diameters down to 2 nm. These QDs are formed during high-temperature dry oxidation of Si/SiGe heterostructure pillars, during which Ge diffuses along the pillars' sidewalls and encapsulates the Si layers. Continued oxidation results in QDs with sizes dependent on oxidation time. The formation of a Ge-rich shell that encapsulates the Si QDs is observed, a configuration which is confirmed to be thermodynamically favorable with molecular dynamics and density functional theory. The type-II band alignment of the Si dot/SiGe pillar suggests that charge trapping on the Si QDs is possible, and electron energy loss spectra show that a conduction band offset of at least 200 meV is maintained for even the smallest Si QDs. Our approach is compatible with current Si-based manufacturing processes, offering a new avenue for realizing Si QD devices.

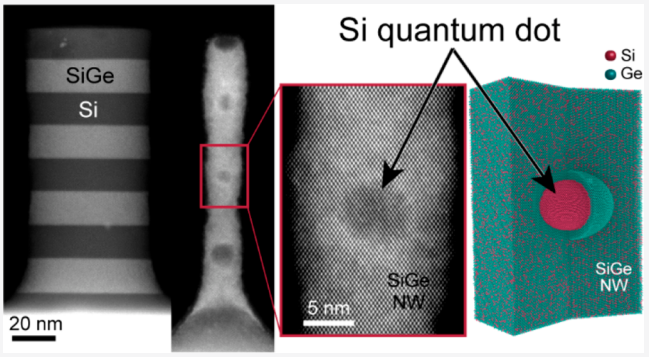

KEYWORDS: *Si quantum dots, Si/SiGe pillars, high-temperature oxidation, vertically stacked QDs*

The ability to fabricate quantum dots (QDs) in a controllable manner compatible with current Si-based manufacturing processes is highly desirable for a wide range of applications including quantum computing,[1−3] optoelectronics,[4−8] and microelectronics.[9,10] One way to ensure such compatibility is to implement QDs from the Si/SiGe materials system through the fabrication of SiGe, Ge, and Si QDs. SiGe QD formation has been accomplished on Si(100) surfaces through a variety of patterning and deposition methods[11−13] as well as through the use of SiGe/Si heterostructures.[13] Ge QDs have also been realized through growth on Si(100) surfaces,[14−18] as well as through controlled oxidation of SiGe nanostructures.[8,19,20] In particular, vertically stacked Ge QDs have been fabricated through SiGe pillar oxidation,[21] with the Ge QD position being controlled via Ge QDs "burrowing" through SiO_2 to reach SiN layers.[22−24] Vertically stacked Si QDs encapsulated in SiO_2 have also been fabricated through oxidation of corrugated Si nanopillars,[25] resulting in stacked Si QDs with visible to near-infrared photoluminescence. However, SiO_2 is limited as an encapsulating material for some QD microelectronics applications in part due to the insulating nature of oxide.

Si QDs encapsulated in a SiGe host may be particularly useful for applications reliant on charge trapping. Due to the type-II band alignment between Si and compressively strained SiGe, a Si QD encapsulated in SiGe can achieve quantum confinement for one or more electrons,[26,27] which is desirable for single-electron transistors, single-photon generation/detection, and qubit devices.[6,27,28] Further, core−shell Si−Ge nanostructures have been shown to offer enhanced performance for a variety of applications.[29−31] We propose the fabrication of core−shell Si−Ge QDs encapsulated in a SiGe host nanowire as an intriguing route to tune QD properties in the Si/SiGe materials system.

In this work, we demonstrate the formation of site-controlled, stacked, strained single-crystal Si QDs encapsulated in vertical SiGe nanowires by leveraging an enhanced Ge diffusion process during thermal oxidation of Si/SiGe nanoheterostructures.[32,33] These Si QDs are tunable in size down to 2 nm, and the fabrication process is compatible with current silicon wafer manufacturing techniques. We also observe a Ge shell surrounding the Si QDs, which we suggest is a thermodynamically favorable result using molecular dynamics (MD) and density functional theory (DFT). In all QDs examined, electron energy loss spectroscopy (EELS) analysis

Received: April 27, 2021
Revised: September 22, 2021
Published: September 28, 2021

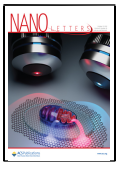

https://doi.org/10.1021/acs.nanolett.1c01670
Nano Lett. 2021, 21, 7905−7912

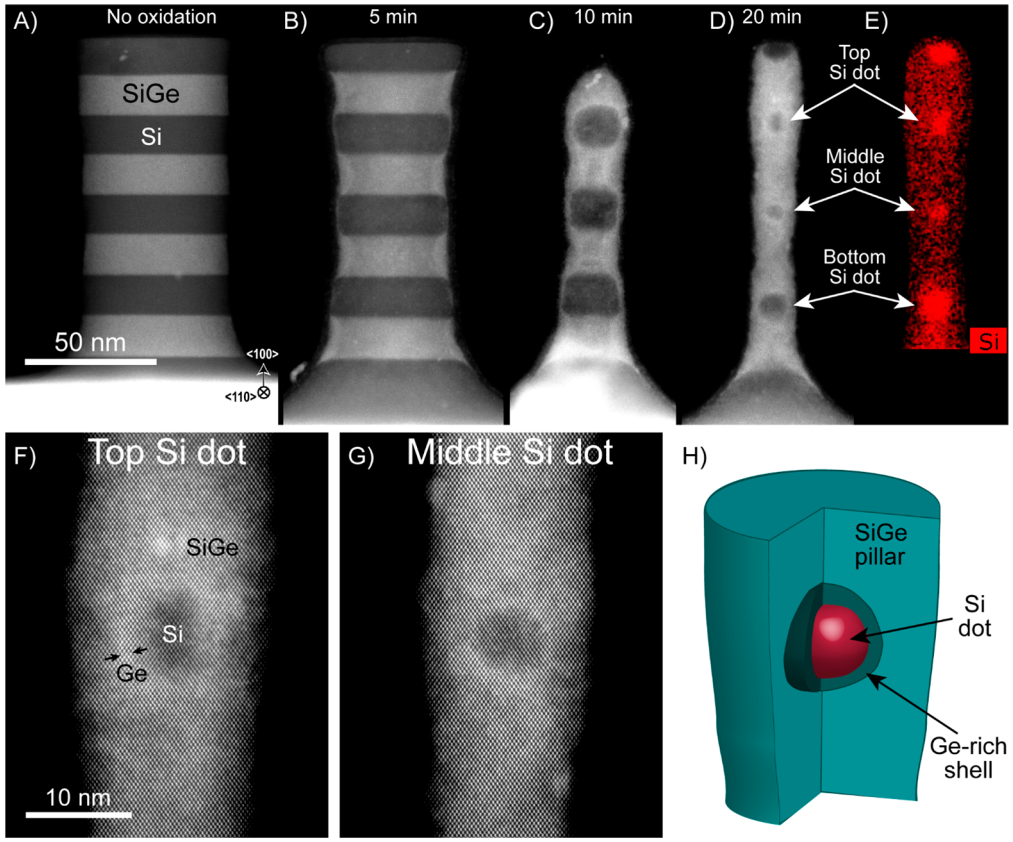

Figure 1. HAADF STEM images of 60 nm-diameter SiGe (light gray)/Si (dark gray) pillars after oxidation under flowing O_2 at 900 °C for (A) 0 min, (B) 5 min, (C) 10 min, and (D) 20 min, demonstrating encapsulated Si dots. The top, middle, and bottom Si dot widths in (D) are 5, 6, and 11 nm, respectively. (E) The Si EDS map corresponding to Figure 1D highlighting three stacked Si dots. (F) A higher magnification of the top Si dot in Figure 1D with the Ge-rich shell surrounding the Si dot highlighted by black arrows. (G) The middle dot of the pillar in 1D with a corresponding graphic shown in (H) demonstrates the 3-D layers present in the nanostructure. The oxide has been removed from the Si/SiGe pillars before imaging for increased resolution.

demonstrates a conduction band offset of at least 200 meV, allowing for charge trapping on the QDs.

Si/SiGe NANOPILLAR FABRICATION

A Si/SiGe superlattice was grown on a 300 mm n-type Si(100) wafer with alternating layers of 15 nm-thick Si and pseudomorphic $Si_{1-x}Ge_x$ layers (x = 0.3). Four layers each of Si and SiGe were grown for a total Si/SiGe stack height of 120 nm. Vertical pillars were defined using e-beam lithography and deep reactive ion etching (DRIE), resulting in 120 nm-tall features with initial diameters ranging from 25 to 200 nm (additional details in the Supporting Information). A conventional tube furnace at 900 °C with flowing O_2 was used to oxidize each sample for a different amount of time to create a time series. Additional deposited oxide protected the pillars during focused ion beam cross-section preparation and allowed for subsequent removal of all material surrounding the pillars using a wet-chemical etch method developed for cross-sectional transmission electron microscopy (TEM) of 3-D nanostrucutres.[34]

Si QD FORMATION VIA HIGH-TEMPERATURE OXIDATION

The evolution of 60 nm-diameter pillars during oxidation is shown in cross-section using high-angle annular dark-field (HAADF) scanning transmission electron microscopy (STEM) images in Figure 1. After a 5 min oxidation (Figure 1B), a thin SiGe layer forms along the sidewalls of the pillar, resulting in encapsulated Si discs. Increasing oxidation time results in these discs becoming more spherical and decreasing in diameter as shown in Figure 1C. Continued oxidation further reduces the size of these Si dots while still retaining a defined, extended defect-free Si dot interface as shown in Figure 1D. Figure 1E shows STEM energy dispersive X-ray spectroscopy (EDS) Si K mapping of the 20 min oxidized pillar, highlighting the formation of three stacked, single-crystal Si QDs encapsulated in the vertical SiGe nanowire. With this result, we demonstrate the ability to tune the Si dot size through oxidation time. With continued oxidation, we achieve Si QD sizes down to approximately 2 nm in diameter. EELS Si compositional mapping of a 2 nm-diameter Si QD is available in the Supporting Information. We note that the initial diameter of the pillar used for Figure 1B was approximately 20% larger than the other pillars in the series, so while the Ge sidewall behavior is a good representation of the pillar evolution, the absolute diameter of the 5 min oxidation sample is not indicative of 60 nm-diameter pillar oxidation. Also of note, the pillar in Figure 1C was slightly overetched during the DRIE, leading to loss of the topmost Si layer.

The pillar sidewall shape evolves during oxidation, gradually becoming concave as oxidation time continues and affecting the Si QD dimensions. Previous work studying the oxidation of Si nanopillars revealed slower oxidation rates at the top and bottom of pillars due to curvature effects.[35] A similar

https://doi.org/10.1021/acs.nanolett.1c01670
Nano Lett. 2021, 21, 7905−7912

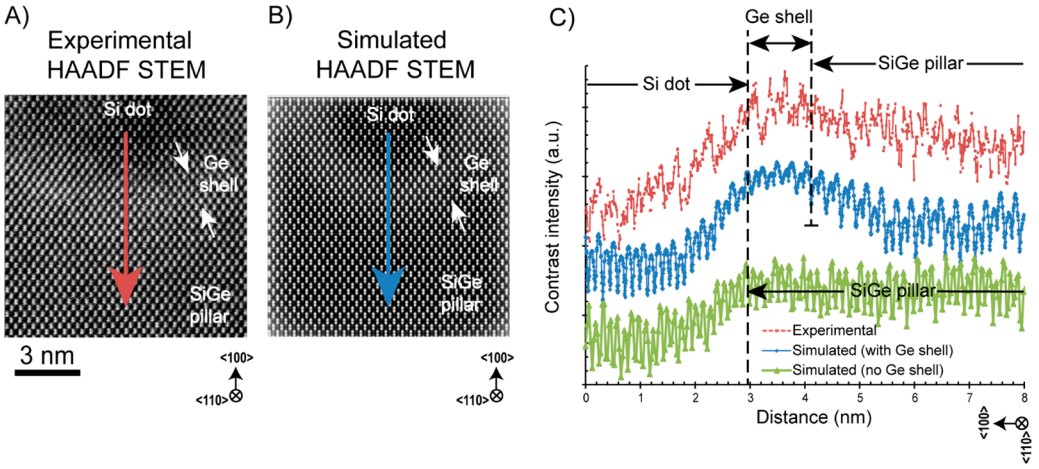

Figure 2. HAADF STEM images of the bottom half of a Si dot, Ge shell, and SiGe pillar after a 35 min oxidation at 900 °C with (A) the experimental image and (B) the simulated image. (C) Graph of the gray values of the STEM images along the lines drawn in parts (A) and (B) of the experimental (top red line) and the simulated (middle blue line) results, with zero distance corresponding to the top of the STEM image. The simulated STEM image without a Ge shell (bottom green line) is also graphed, and the image is available in the SI. The data sets have been offset for clarity, and dashed lines indicate the boundaries of the Si, Ge, and SiGe regions in the models used for the simulated STEM images. Experimental data matches well with a model that includes a Ge shell around the Si dot.

retardation of the oxidation rate at the top and bottom of the Si/SiGe pillars is observed, leading to encapsulated Si dots that evolve at different rates during oxidation. For example, the top Si dot shown in Figure 1F is slightly larger than the middle dot shown in Figure 1G, likely due to the higher oxidation rate at the middle of the pillar when compared with the top or bottom of the pillar. If necessary, it may be possible to mitigate this effect through a multiple-step oxidation in the self-limiting oxidation regime[36,37] such as that done by Ye et al. to reduce variations in Si nanopillar oxidation[38] or by placing the Si layers further from the substrate via a deeper RIE.

SiGe oxidation is known to occur in a similar fashion to Si oxidation, with the new oxide layer forming at the oxide/SiGe interface. Prior studies report a temperature regime from ~800−1000 °C for SiGe oxidation that selectively oxidizes Si, creating a Ge-rich pile-up layer in the SiGe at the SiGe/SiO_2 interface.[39−43] Continued oxidation results in further increase of the Ge concentration in the SiGe. To investigate the composition of our pillars, EDS and EELS analysis were used to reveal Ge concentrations up to 80% in the SiGe after oxidation (compared to the initial 30% Ge concentration). Our nanostructures remain dislocation-free despite the lattice mismatch between Si and $Si_{0.2}Ge_{0.8}$.[44] A possible explanation is that some strain relaxation has occurred through elastic deformation due to high free surface area of the nanowires,[45] rather than plastic deformation as would be evidenced by dislocations.

INVESTIGATION OF A Ge SHELL AROUND A Si QD

Interestingly, a bright halo suggesting higher Ge content around the encapsulated Si QD is observed during longer oxidation times as indicated by black arrows in Figure 1F and the illustration in Figure 1H. Other sources besides compositional differences can also cause intensity variation in STEM imaging of crystalline materials, including strain fields and sample thickness variations. While strain is known to affect the contrast in ADF STEM, the intensity changes due to strain are highly dependent on the detector angle.[46] In HAADF STEM images, the intensity changes due to strain are small and the lattice bending due to strain causes decreased, not increased, intensity due to dechanneling of the electron probe.[47−49] Increased sample thickness for STEM images leads to an increase in detected intensity,[50−52] so to minimize thickness variation while investigating the bright halo around the Si dot we compare gray value intensities in the STEM images along the vertical axis of the pillar.

Previous studies have met with success in investigating the interface of core−shell QD structures through a combination of simulation and HAADF STEM imaging.[53] Therefore, to assist in the investigation of the nanostructure composition, HAADF STEM simulations were carried out using SICSTEM software[54] and compared to experimental HAADF STEM images as shown in Figure 2 (additional details in the Supporting Information). A bright, defined shell around the Si dot is experimentally detectable (Figure 2A) through a gray value line scan along the pillar axis as shown by the red dashed line in Figure 2C. The line scan through the simulated STEM image from a model with a Ge shell (Figure 2B) is shown by the blue line in Figure 2C, and the results from a model without a Ge shell are shown by the green line. As both models include strain, a good agreement between the experimental and Ge-shell simulation data suggests that a Ge-rich shell, and not strain, is the cause of the change in intensity for the experimental STEM image.

Similar Ge behavior was also observed by Di et al. while oxidizing a SiGe-on-insulator (SGOI) material system, where Ge pile-up was seen at the oxidizing interface as well as at the SiGe/buried-oxide (BOX) interface for long oxidation times.[55] Di et al. speculated that the second pile-up region at the SiGe/BOX interface was due to a combination of the Ge rejection at the oxidizing surface and the slow rate of Ge diffusion into the BOX. The analogous SiGe/BOX interface for our Si/SiGe pillars is the SiGe/Si dot interface, where Ge piles up for long oxidation times in part due to the slow rate of diffusion of Ge into Si.

We also carried out MD and DFT calculations to investigate the favorability of Ge shell formation around an encapsulated Si dot (see Supporting Information for details). From MD calculations, we retrieve an overall energy difference of 10 meV/atom between the Ge shell and no Ge shell structure,

https://doi.org/10.1021/acs.nanolett.1c01670
Nano Lett. 2021, 21, 7905−7912

favoring the formation of a Ge shell. However, this result should be treated with caution as the energy difference is below the size of typical systematic errors in MD simulations. Further, the interatomic potentials in our MD calculations do not explicitly treat the electronic structure of the chemical bonds comprising the interface. Therefore, we use DFT to make an energetic comparison based on a fully quantum mechanical approach to the electronic structure.

Applying DFT to slices of the atomic configurations realized in the MD simulation, we predict an energy difference of 64 meV/atom, again in favor of the Ge shell case. We calculate the entropic contribution to the free energy at room temperature to be approximately 12 meV/atom in favor of mixing within the Ge shell region, leading to a total free energy difference of approximately 50 meV/atom in favor of Ge shell formation. While this energy difference is still within the methodological uncertainty of DFT, multiple chemical tools parametrized at both a classical and quantum mechanical level indicate that Ge shell formation is, in fact, a thermodynamically favored outcome for these Si QDs.

STRAIN AND ELECTRONIC STRUCTURE OF Si QDS

The strain present in the Si dot and surrounding material will affect the band structure and band alignment present in these nanostructures, which will in turn affect the utility of these QDs for many device applications. Conventional experimental methods to determine strain from atomic resolution STEM images using geometric phase analysis are frustrated by the embedded nature of the Si QD. To address this, strain values were extracted from the MD calculations, as shown in Figure 3. Stress on the silicon is hydrostatic and tensile while stress on the Ge shell is nonuniform and compressive. Figure 3A shows the inverse relationship between strain of the Si QDs and QD diameter. Error bars account for variations in strain across the Si QDs. Computational stress maps, as seen in Figure 3B,C, reveal that the vast majority of stress on the system is placed on the Si dot and surrounding Ge shell with stress in the surrounding SiGe rapidly approaching zero. The stress map of a 10 nm-diameter Si dot is available in the Supporting Information. As the ratio of the Si dot to SiGe pillar diameter becomes larger, the Si lattice parameters appear to dominate, leading to roughly zero lattice strain in the Si for the 16 and 23 nm-diameter Si dots.

The electronic structure of our strained Si QDs differs significantly from bulk Si due to the presence of both strain and quantum confinement. To investigate this, monochromated EELS inside a 60 kV STEM was used to measure high-resolution Si $L_{2,3}$ edges for the embedded Si QDs. The near-edge fine structure in these spectra, shown in Figure 4, is a direct measure of the unoccupied conduction band (CB) density of states.[56] Figure 4A shows the spin-3/2 component of the $L_{2,3}$ spectra, after background removal, of the portion of the Si/SiGe nanostructure with only SiGe as well as the portion of the Si/SiGe nanostructure with the embedded Si dot/Ge shell (Supporting Information). Figure 4B is the L_3 spectra of just the Si dots, a result of subtracting the SiGe pillar/Ge shell contribution from the Si dot/Ge shell/SiGe pillar spectra. The inflection points, indicated by red markers, give the energy of the conduction band minima (CBM).[57] We see a large difference of approximately 350 meV in onset energy between the $Si_{0.2}Ge_{0.8}$ pillar and Si substrate spectra, suggesting a type-II band alignment that would allow charge trapping on the Si QDs. We see that the near-edge structures

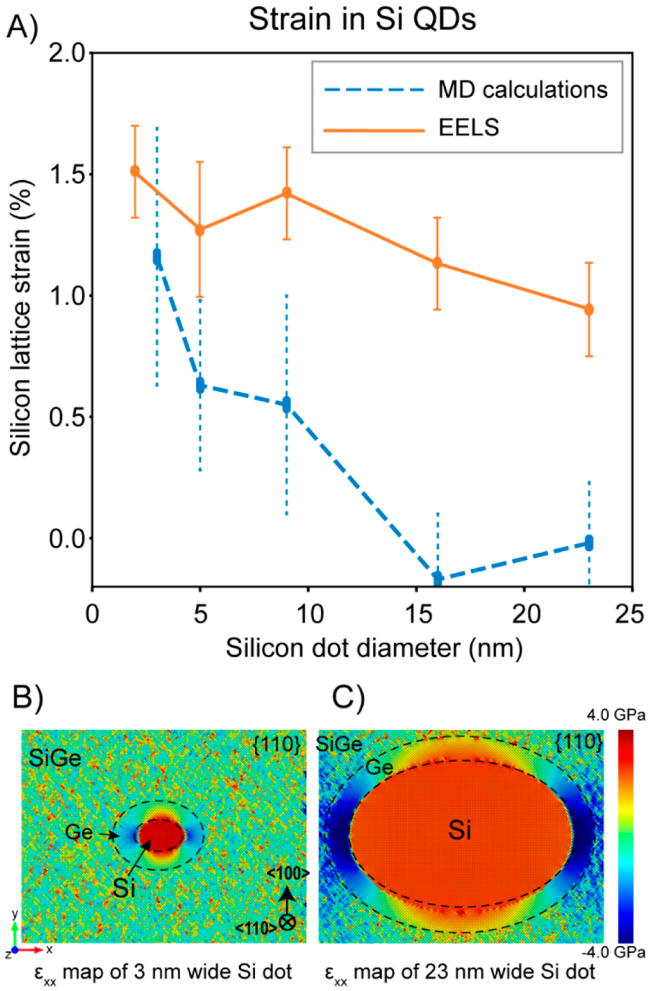

Figure 3. Strain calculations for a range of Si dot sizes using molecular dynamics (MD) and electron energy loss spectroscopy (EELS). (A) MD simulations (blue dashed line) and strain calculated from EELS (orange line) show a trend for higher strain as the dot diameter decreases. Computational stress maps for (B) a 3 nm wide Si dot and (C) a 23 nm wide Si dot reveal higher levels of stress in the smaller Si dot and a fairly even distribution of stress within each QD.

of the Si QDs resemble that of bulk unstrained Si, suggesting that our QDs are under hydrostatic strain and no splitting of CB valleys has occurred.[57]

The Si QD energy shift consists of three contributions as illustrated in Figure 5: a strain-dependent shift in the 2p core levels, a strain-dependent shift in the Si Δ valleys, and a shift due to quantum confinement for electrons occupying the Si QDs under a type-II band alignment. The two strain-dependent shifts push the respective energy levels in opposite directions, increasing the relevant transition energy under hydrostatic tensile strain. The effect of confinement also tends to increase the relevant transition energy and only implicitly depends on strain in that the relevant band offsets depend on strain.

To compare with the MD calculations, we estimate the magnitude of the strain in our Si QDs using EELS data. By employing the equation shown in Figure 5, with an estimated 2p core level shift of 6 eV[58] and the aggregate shift in the Si ΔCBM due to the dilatation and uniaxial deformation potentials inferred as 4.6 eV,[59] we expect that a 1% hydrostatic tensile strain will result in a 106 meV shift in the transition

https://doi.org/10.1021/acs.nanolett.1c01670
Nano Lett. 2021, 21, 7905−7912

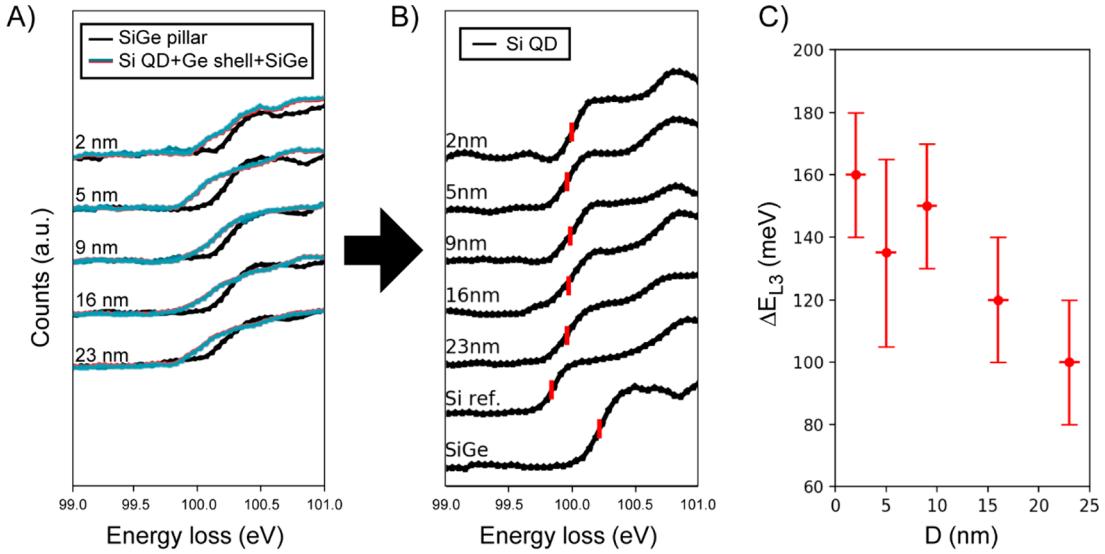

Figure 4. EELS data for a range of Si QD diameters encapsulated in SiGe pillars. (A) L_3 spectra for the SiGe pillar and for the Si QD/Ge shell/SiGe pillar nanostructure for varying sizes of Si QD diameters. (B) L_3 spectra for Si QDs with varying sizes are shown, with bulk unstrained Si (Si ref.) and $Si_{0.2}Ge_{0.8}$ (SiGe) as labeled. The red markers highlight the inflection point of each edge onset. (C) The change in energy of the Si L_3 edge onset is shown as a function of Si QD diameter (D).

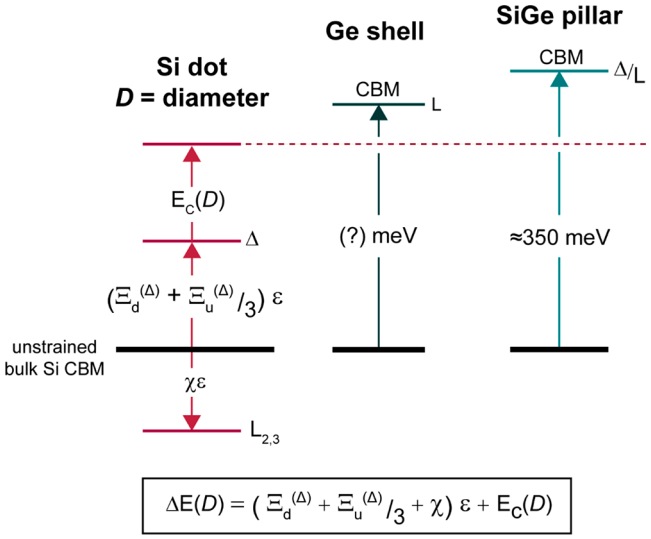

Figure 5. Conduction band minimum (CBM) offsets for the Si dot, Ge shell, and SiGe pillar. The shift in the Δ valleys of the Si dot due to hydrostatic strain is given by the product of the strain and a particular combination of the dilatation ($\Xi_d^{(\Delta)}$) and uniaxial ($\Xi_u^{(\Delta)}$) deformation potentials. The total shift in the energies of bound states in the Si dot is then given by the sum of this strain-dependent shift in the Δ valleys, the shift in core-level energies due to strain ($\chi\varepsilon$), and the shift due to quantum confinement ($E_C(D)$). Relative offsets from bulk Si for the Ge shell (unknown) and the $Si_{0.2}Ge_{0.8}$ pillar (≈350 meV) are illustrated.

energy probed by EELS relative to bulk Si. If we neglect the effect of quantum confinement, the strain in our Si QDs calculated using EELS data is shown in Figure 3A. While this estimate of the strain is fairly consistent with the MD calculations for the smaller dots, the strain in the larger dots significantly deviates from the MD calculations. While quantum confinement may play a role in shifting the Si QD $L_{2,3}$ spectra, a lack of direct constraints on the electronic structure of the Ge-rich shell around the Si QDs makes calculating this effect difficult.

To understand the band alignments of the Si QD, Ge shell, and SiGe pillar, we first turn to our EELS measurements, which indicate that the conduction band offset (CBO) between the Si QD and the surrounding SiGe is at least 200 meV. However, we do not know what the relevant offset is between the Si dot and the Ge shell. Further, the inhomogeneous nature of the strain in the Ge shell predicted by our classical MD calculations suggests that the band offset and the valley structure of the relevant conduction band minima in the Ge shell might be highly nonuniform. To estimate how large the Si dot/Ge shell band offset might be, we employ a simple effective mass model in which each region is characterized by a constant potential and the effective mass of a single bulk-like valley (Δ in the Si QD, L in the Ge shell). We fix the CBO between Si and SiGe to 200 meV and allow the offset between Si and Ge to vary to rationalize the observed EELS shift and the strains predicted by classical MD. For the 2 and 5 nm Si QDs, we predict the Ge shell would need to be offset 150 meV below and 5 meV below the Si QD, respectively, in order to bind an electron to the QD. Details are given in Supporting Information.

Using this model, we are able to tentatively estimate the strain at approximately 1% for all of our QDs, but further analysis is needed to sharpen our understanding of this system. The strain-dependent 2p core level shift, the CBO between the Si core and Ge shell, and the inhomogeneous nature of the strain in the shell all need to be more precisely constrained. Atomistic tight-binding calculations may be a promising modeling tool to resolve ambiguities in our analysis and to help better understand both the EELS and the opportunities for optoelectronic applications in this novel system.

CONCLUSIONS

We demonstrate for the first time that enhanced lateral diffusion of Ge along all sides of Si/SiGe superlattice nanopillars occurs during oxidation, enabling the formation of Si QDs embedded in extended defect-free SiGe nanowires with QD diameters down to 2 nm. In addition, a Ge-rich shell is observed to form around the QD. EELS analysis confirms a

https://doi.org/10.1021/acs.nanolett.1c01670
Nano Lett. 2021, 21, 7905−7912

type-II band alignment between the Si QD and the surrounding SiGe pillar, as well as a shift in the Si $L_{2,3}$ edge that is dependent on the QD size. This L edge shift suggests that the combined effects of strain and quantum confinement cause a reduction in the potential well present in the Si QD. However, the estimated 200 meV potential well is still deep enough to allow trapping of an electron on the Si QD, a key property for memory or logic applications. While the predicted ~1% strain in our QDs may not be sufficient to shift the Γ and Δ valley bands enough to achieve direct bandgap behavior, the quantized states in the Si QDs may suppress phonon recombination and allow the direct gap behavior to dominate,[60,61] but further investigation is needed. The ability to stack a desired number of Si QDs in a SiGe pillar, as well as tune the distance between these dots by changing the initial thickness of the SiGe layers, may allow these Si QDs to interact with one another, which may be useful for quantum computing applications. These techniques could potentially be extended to create novel shapes such as rings, ovals, and crossed wires. Existing processes for device fabrication, such as techniques for establishing contacts to vertical nanostructures,[62−64] are compatible with our oxidized Si/SiGe nanostructures. In sum, our demonstrated ability to fabricate site-specific, extended defect-free Si QDs of controllable size could enable a broad array of applications in the field of optoelectronics, QD memory and logic devices, and quantum computing.

■ ASSOCIATED CONTENT

Supporting Information

The Supporting Information is available free of charge at https://pubs.acs.org/doi/10.1021/acs.nanolett.1c01670.

Sample preparation, STEM EELS, SICSTEM simulations, MD calculations, DFT calculations, and theoretical electronic structure calculations (PDF)

■ AUTHOR INFORMATION

Corresponding Authors

Emily M. Turner − *Department of Materials Science and Engineering, University of Florida, Gainesville, Florida 32611, United States;* orcid.org/0000-0001-7210-7606; Email: emilymturner@ufl.edu

Kevin S. Jones − *Department of Materials Science and Engineering, University of Florida, Gainesville, Florida 32611, United States*; Email: kjones@eng.ufl.edu

George T. Wang − *Advanced Materials Sciences Department, Sandia National Laboratories, Albuquerque, New Mexico 87158, United States;* orcid.org/0000-0001-9007-0173; Email: gtwang@sandia.gov

Authors

Quinn Campbell − *Quantum Computer Science Department, Sandia National Laboratories, Albuquerque, New Mexico 87158, United States;* orcid.org/0000-0003-1377-3769

Joaquín Pizarro − *Department of Computer Engineering, University of Cádiz, Puerto Real 11519, Spain*

Hongbin Yang − *Department of Chemistry and Chemical Biology, Rutgers University, Piscataway, New Jersey 08854, United States;* orcid.org/0000-0002-0098-6944

Keshab R. Sapkota − *Advanced Materials Sciences Department, Sandia National Laboratories, Albuquerque, New Mexico 87158, United States;* orcid.org/0000-0001-8581-4211

Ping Lu − *Department of Materials Characterization and Performance, Sandia National Laboratories, Albuquerque, New Mexico 87158, United States*

Andrew D. Baczewski − *Quantum Computer Science Department, Sandia National Laboratories, Albuquerque, New Mexico 87158, United States*

Complete contact information is available at: https://pubs.acs.org/10.1021/acs.nanolett.1c01670

Author Contributions

E.M.T, K.S.J., and G.T.W. conceived the concept and design of the experiment. E.M.T fabricated and processed the Si/SiGe pillars. K.R.S. assisted in quantum device discussions. J.P. provided SICSTEM simulations of the Si dot/Ge shell/SiGe pillar system. H.Y. collected EELS spectra and composition maps for a range of Si/SiGe pillars. Q.C. and A.D.B. provided theoretical analysis, including MD and DFT simulations. P.L. gathered aberration-corrected HAADF STEM images as well as EDS data. The manuscript was written through contributions of all authors, and all authors have given approval to the final version of the manuscript.

Funding

This work was supported by the Laboratory Directed Research and Development program at Sandia National Laboratories, a multimission laboratory managed and operated by National Technology and Engineering Solutions of Sandia, LLC., a wholly owned subsidiary of Honeywell International, Inc., for the U.S. Department of Energy's National Nuclear Security Administration under contract DE-NA-0003525. This work was performed, in part, at the Center for Integrated Nanotechnologies, a U.S. Department of Energy, Office of Basic Energy Sciences user facility. This paper describes objective technical results and analysis. Any subjective views or opinions that might be expressed in the paper do not necessarily represent the views of the U.S. Department of Energy or the United States Government.

Notes

The authors declare no competing financial interest.
DFT and MD input files are available upon request.

■ ACKNOWLEDGMENTS

We gratefully acknowledge Toby Jacobson for his contributions to our entropy calculations and thoughtful discussions around modeling the Si dot/SiGe pillar system. We also acknowledge Ezra Bussmann for critical reading of the manuscript. H.Y. acknowledges discussions with Profs. E. Garfunkel and P. Batson on EELS analysis.

■ ABBREVIATIONS

BOX, buried-oxide; CBM, conduction band minimum; CBO, conduction band offset; DFT, density functional theory; DRIE, deep reactive ion etch; EDS, energy dispersive X-ray spectroscopy; EELS, electron energy loss spectroscopy; HAADF, high-angle annular dark-field; MD, molecular dynamics; QD, quantum dot; SGOI, SiGe-on-insulator; STEM, scanning transmission electron microscopy; TEM, transmission electron microscopy

■ REFERENCES

(1) Morton, J. J. L.; McCamey, D. R.; Eriksson, M. A.; Lyon, S. A. Embracing the Quantum Limit in Silicon Computing. *Nature* **2011**, *479*, 345−353.

(2) Kawakami, E.; Scarlino, P.; Ward, D. R.; Braakman, F. R.; Savage, D. E.; Lagally, M. G.; Friesen, M.; Coppersmith, S. N.; Eriksson, M. A.; Vandersypen, L. M. K. Electrical Control of a Long-Lived Spin Qubit in a Si/SiGe Quantum Dot. *Nat. Nanotechnol.* **2014**, *9*, 666−670.
(3) Zajac, D. M.; Sigillito, A. J.; Russ, M.; Borjans, F.; Taylor, J. M.; Burkard, G.; Petta, J. R. Resonantly Driven CNOT Gate for Electron Spin. *Science* **2018**, *359*, 439−442.
(4) Dohnalová, K.; Poddubny, A. N.; Prokofiev, A. A.; De Boer, W. D.; Umesh, C. P.; Paulusse, J. M.; Zuilhof, H.; Gregorkiewicz, T. Surface Brightens up Si Quantum Dots: Direct Bandgap-like Size-Tunable Emission. *Light: Sci. Appl.* **2013**, *2* (1), e47.
(5) Poddubny, A. N.; Dohnalová, K. Direct Band Gap Silicon Quantum Dots Achieved via Electronegative Capping. *Phys. Rev. B: Condens. Matter Mater. Phys.* **2014**, *90* (24), 245439.
(6) Baykan, M. O.; Thompson, S. E.; Nishida, T. Strain Effects on Three-Dimensional, Two-Dimensional, and One-Dimensional Silicon Logic Devices: Predicting the Future of Strained Silicon. *J. Appl. Phys.* **2010**, *108* (9), 093716.
(7) Kůsová, K.; Hapala, P.; Valenta, J.; Jelínek, P.; Cibulka, O.; Ondič, L.; Pelant, I. Direct Bandgap Silicon: Tensile-Strained Silicon Nanocrystals. *Adv. Mater. Interfaces* **2014**, *1*, 1300042.
(8) Liao, P. H.; Kuo, M. H.; Tien, C. W.; Chang, Y. L.; Hong, P. Y.; George, T.; Lin, H. C.; Li, P. W. Self-Organized Gate Stack of Ge Nanosphere/SiO2/Si1-XGex Enables Ge-Based Monolithically-Integrated Electronics and Photonics on Si Platform. In *Symposium on VLSI Circuits Digest of Technical Papers*; IEEE: 2018; pp 157−158.
(9) Dhungana, K. B.; Jaishi, M.; Pati, R. Unlocking the Origin of Superior Performance of a Si−Ge Core−Shell Nanowire Quantum Dot Field Effect Transistor. *Nano Lett.* **2016**, *16*, 3995−4000.
(10) Lavieville, R.; Triozon, F.; Barraud, S.; Corna, A.; Jehl, X.; Sanquer, M.; Li, J.; Abisset, A.; Duchemin, I.; Niquet, Y. M. Quantum Dot Made in Metal Oxide Silicon-Nanowire Field Effect Transistor Working at Room Temperature. *Nano Lett.* **2015**, *15*, 2958−2964.
(11) Amatya, J. M.; Floro, J. A. Site-Selection of $Si_{1-x}Ge_x$ Quantum Dots on Patterned Si(001) Substrates. *Appl. Phys. Lett.* **2016**, *109* (19), 193112.
(12) Brehm, M.; Grydlik, M. Site-Controlled and Advanced Epitaxial Ge/Si Quantum Dots: Fabrication, Properties, and Applications. *Nanotechnology* **2017**, *28*, 392001.
(13) Dais, C.; Mussler, G.; Fromherz, T.; Müller, E.; Solak, H. H.; Grützmacher, D. SiGe Quantum Dot Crystals with Periods down to 35 Nm. *Nanotechnology* **2015**, *26*, 255302.
(14) Ma, Y. J.; Zhong, Z.; Yang, X. J.; Fan, Y. L.; Jiang, Z. M. Factors Influencing Epitaxial Growth of Three-Dimensional Ge Quantum Dot Crystals on Pit-Patterned Si Substrate. *Nanotechnology* **2013**, *24* (1), 015304.
(15) Chen, K. H.; Chien, C. Y.; Lai, W. T.; George, T.; Scherer, A.; Li, P. W. Controlled Heterogeneous Nucleation and Growth of Germanium Quantum Dots on Nanopatterned Silicon Dioxide and Silicon Nitride Substrates. *Cryst. Growth Des.* **2011**, *11* (7), 3222−3226.
(16) Wang, S.; Zhou, T.; Li, D.; Zhong, Z. Evolution and Engineering of Precisely Controlled Ge Nanostructures on Scalable Array of Ordered Si Nano-Pillars. *Sci. Rep.* **2016**, *6*, 28872.
(17) Ye, F. F.; Ma, Y. J.; Lv, Y.; Jiang, Z. M.; Yang, X. J. Investigating the Composition and Conductance Distributions on Highly GeSi Mixed Quantum Dots and Inside Oxidation Problem. *Nanoscale Res. Lett.* **2011**, *10*, 476.
(18) Chen, H. M.; Suen, Y. W.; Chen, S. J.; Luo, G. L.; Lai, Y. P.; Chen, S. T.; Lee, C. H.; Kuan, C. H. Effect of Surface Si Redistribution on the Alignment of Ge Dots Grown on Pit-Patterned Si(001) Substrates. *Nanotechnology* **2014**, *25*, 475301.
(19) Kuo, M. H.; Wang, C. C.; Lai, W. T.; George, T.; Li, P. W. Designer Ge Quantum Dots on Si: A Heterostructure Configuration with Enhanced Optoelectronic Performance. *Appl. Phys. Lett.* **2012**, *101* (22), 223107.
(20) Peng, K. P.; Chen, C. L.; Tang, Y. T.; Kuo, D.; George, T.; Lin, H. C.; Li, P. W. Self-Organized Pairs of Ge Double Quantum Dots with Tunable Sizes and Spacings Enable Room-Temperature Operation of Qubit and Single-Electron Devices. In *2019 IEEE International Electron Devices Meeting (IEDM)*; IEEE: 2019; pp 37.4.1−37.4.4.
(21) Wang, C. C.; Chen, K. H.; Chen, I. H.; Lai, W. T.; Chang, H. T.; Chen, W. Y.; Hsu, J. C.; Lee, S. W.; Hsu, T. M.; Hung, M. T.; Li, P. W. CMOS-Compatible Generation of Self-Organized 3-D Ge Quantum Dot Array for Photonic and Thermoelectric Applications. *IEEE Trans. Nanotechnol.* **2012**, *11* (4), 657−660.
(22) Wang, C.-C.; Liao, P.-H.; Kuo, M.-H.; George, T.; Li, P.-W. The Curious Case of Exploding Quantum Dots: Anomalous Migration and Growth Behaviors of Ge under Si Oxidation. *Nanoscale Res. Lett.* **2013**, *8*, 192.
(23) George, T.; Li, P. W.; Chen, K. H.; Peng, K. P.; Lai, W. T. 'Symbiotic' Semiconductors: Unusual and Counter-Intuitive Ge/Si/O Interactions. *J. Phys. D: Appl. Phys.* **2017**, *50* (10), 105101.
(24) Huang, T. L.; Peng, K. P.; Chen, C. L.; Lin, H. C.; George, T.; Li, P. W. Tunable Diameter and Spacing of Double Ge Quantum Dots Using Highly-Controllable Spacers and Selective Oxidation of SiGe. *Sci. Rep.* **2019**, *9* (1), 11303.
(25) Walavalkar, S. S.; Homyk, A. P.; Hofmann, C. E.; Henry, M. D.; Shin, C.; Atwater, H. A.; Scherer, A. Size Tunable Visible and Near-Infrared Photoluminescence from Vertically Etched Silicon Quantum Dots. *Appl. Phys. Lett.* **2011**, *98* (15), 153114.
(26) Nayak, D. K.; Usami, N.; Fukatsu, S.; Shiraki, Y. Band-Edge Photoluminescence of SiGe/Strained-Si/SiGe Type-II Quantum Wells on Si(100). *Appl. Phys. Lett.* **1993**, *63* (25), 3509−3511.
(27) Lockwood, D. J.; Wu, X.; Baribeau, J.-M.; Mala, S. A.; Wang, X.; Tsybeskov, L. Si/SiGe Heterointerfaces in One-, Two-, and Three-Dimensional Nanostructures: Their Effect on SiGe Light Emission. *Front. Mater.* **2016**, *3*, 12.
(28) Srinivasan, S.; Klimeck, G.; Rokhinson, L. P. Valley Splitting in Si Quantum Dots Embedded in SiGe. *Appl. Phys. Lett.* **2008**, *93* (11), 112102.
(29) de Oliveira, E. L.; Albuquerque, E. L.; de Sousa, J. S.; Farias, G. A.; Peeters, F. M. Configuration-Interaction Excitonic Absorption in Small Si/Ge and Ge/Si Core/Shell Nanocrystals. *J. Phys. Chem. C* **2012**, *116*, 4399−4407.
(30) Lauhon, L. J.; Gudiksen, M. S.; Wang, D.; Lieber, C. M. Epitaxial Core − Shell and Core − Multishell Nanowire Heterostructures. *Nature* **2002**, *420*, 57−61.
(31) David, T.; Liu, K.; Ronda, A.; Favre, L.; Abbarchi, M.; Gailhanou, M.; Gentile, P.; Buttard, D.; Calvo, V.; Amato, M.; Aqua, J. N.; Berbezier, I. Tailoring Strain and Morphology of Core-Shell SiGe Nanowires by Low-Temperature Ge Condensation. *Nano Lett.* **2017**, *17* (12), 7299−7305.
(32) Brewer, W. M.; Xin, Y.; Hatem, C.; Diercks, D.; Truong, V. Q.; Jones, K. S. Lateral Ge Diffusion During Oxidation of Si/SiGe Fins. *Nano Lett.* **2017**, *17* (4), 2159−2164.
(33) Mertens, H.; Ritzenthaler, R.; Pena, V.; Santoro, G.; Kenis, K.; Schulze, A.; Litta, E. D.; Chew, S. A.; Devriendt, K.; Chiarella, T.; Demuynck, S.; Yakimets, D.; Jang, D.; Spessot, A.; Eneman, G.; Dangol, A.; Lagrain, P.; Bender, H.; Sun, S.; Kim, N.; Barla, K.; Mocuta, D.; Horiguchi, N.; Chiarella, R.; Demuynck, S.; Yakimets, D.; Jang, D.; Spessot, A.; Eneman, G.; Dangol, A.; Lagrain, P.; Bender, H.; Sun, S.; Korolik, M.; Kioussis, D.; Kim, M.; Bu, K.-. H.; Chen, S. C.; Cogorno, M.; Devrajan, J.; Machillot, J.; Yoshida, N.; Kim, N.; Barla, K.; Mocuta, D.; Horiguchi, N. Vertically Stacked Gate-All-Around Si Nanowire Transistors: Key Process Optimizations and Ring Oscillator Demonstration. In *Electron Devices Meeting (IEDM)*; IEEE: 2017; pp 828−831.
(34) Turner, E. M.; Sapkota, K. R.; Hatem, C.; Lu, P.; Wang, G. T.; Jones, K. S. Wet-Chemical Etching of FIB Lift-out TEM Lamellae for Damage-Free Analysis of 3-D Nanostructures. *Ultramicroscopy* **2020**, *216*, 113049.
(35) Ye, S.; Endoh, T. Edge Effect in the Oxidation of Three-Dimensional Nano-Structured Silicon. *Mater. Sci. Semicond. Process.* **2019**, *93*, 266−273.

https://doi.org/10.1021/acs.nanolett.1c01670
Nano Lett. 2021, 21, 7905−7912

(36) Cui, H.; Wang, C. X.; Yang, G. W. Origin of Self-Limiting Oxidation of Si Nanowires. *Nano Lett.* **2008**, *8* (9), 2731−2737.
(37) Ye, S.; Yamabe, K.; Endoh, T. Low-Density Oxide Grown Thermally on Sidewall of Si Nanopillars. *Mater. Lett.* **2020**, *258*, 126780.
(38) Ye, S.; Yamabe, K.; Endoh, T. Variance Reduction during the Fabrication of Sub-20 Nm Si Cylindrical Nanopillars for Vertical Gate-All-Around Metal-Oxide Semiconductor Field-Effect Transistors. *ACS Omega* **2019**, *4*, 21115−21121.
(39) Margalit, S.; Bar-Lev, A.; Kuper, A. B.; Aharoni, H.; Neugroschel, A. Oxidation of Silicon-Germanium Alloys. *J. Cryst. Growth* **1972**, *17*, 288−297.
(40) LeGoues, F. K.; Rosenberg, R.; Nguyen, T.; Himpsel, F.; Meyerson, B. S. Oxidation Studies of SiGe. *J. Appl. Phys.* **1989**, *65* (4), 1724−1727.
(41) Ganster, P.; Saul, A.; Treglia, G. Atomistic Model for Ge Condensation under SiGe Oxidation. *Defect Diffus. Forum* **2015**, *363*, 210−216.
(42) Long, E.; Galeckas, A.; Kuznetsov, A. Y. Ge Concentrations in Pile-up Layers of Sub-100-Nm SiGe Films for Nano-Structuring by Thermal Oxidation. *J. Vac. Sci. Technol., B: Nanotechnol. Microelectron.: Mater., Process., Meas., Phenom.* **2012**, *30* (4), 041212.
(43) Paine, D. C.; Caragianis, C.; Schwartzman, A. F. Oxidation of $Si_{1-x}Ge_x$ Alloys at Atmospheric and Elevated Pressure. *J. Appl. Phys.* **1991**, *70* (9), 5076−5084.
(44) People, R.; Bean, J. C. Calculation of Critical Layer Thickness versus Lattice Mismatch for Ge_xSi_{1-x}/Si Strained-Layer Heterostructures. *Appl. Phys. Lett.* **1985**, *47* (3), 322−324.
(45) Isa, F.; Jung, A.; Salvalaglio, M.; Dasilva, Y. A. R.; Marozau, I.; Meduňa, M.; Barget, M.; Marzegalli, A.; Isella, G.; Erni, R.; Pezzoli, F.; Bonera, E.; Niedermann, P.; Sereda, O.; Gröning, P.; Montalenti, F.; von Känel, H. Strain Engineering in Highly Mismatched SiGe/Si Heterostructures. *Mater. Sci. Semicond. Process.* **2017**, *70*, 117−122.
(46) Hillyard, S.; Silcox, J. Detector Geometry, Thermal Diffuse Scattering and Strain Effects in ADF STEM Imaging. *Ultramicroscopy* **1995**, *58*, 6−17.
(47) Yu, Z.; Muller, D. A.; Silcox, J. Study of Strain Fields at A-Si/c-Si Interface. *J. Appl. Phys.* **2004**, *95* (7), 3362−3371.
(48) Rosenauer, A.; Mehrtens, T.; Müller, K.; Gries, K.; Schowalter, M.; Venkata Satyam, P.; Bley, S.; Tessarek, C.; Hommel, D.; Sebald, K.; Seyfried, M.; Gutowski, J.; Avramescu, A.; Engl, K.; Lutgen, S. Composition Mapping in InGaN by Scanning Transmission Electron Microscopy. *Ultramicroscopy* **2011**, *111*, 1316−1327.
(49) Beyer, A.; Duschek, L.; Belz, J.; Oelerich, J. O.; Jandieri, K.; Volz, K. Influence of Surface Relaxation of Strained Layers on Atomic Resolution ADF Imaging. *Ultramicroscopy* **2017**, *181*, 8−16.
(50) Hillyard, S.; Loane, R. F.; Silcox, J. Annular Dark-Field Imaging: Resolution and Thickness Effects. *Ultramicroscopy* **1993**, *49*, 14−25.
(51) Kotaka, Y. Essential Experimental Parameters for Quantitative Structure Analysis Using Spherical Aberration-Corrected HAADF-STEM. *Ultramicroscopy* **2010**, *110*, 555−562.
(52) Van den Broek, W.; Rosenauer, A.; Goris, B.; Martinez, G. T.; Bals, S.; Van Aert, S.; Van Dyck, D. Correction of Non-Linear Thickness Effects in HAADF STEM Electron Tomography. *Ultramicroscopy* **2012**, *116*, 8−12.
(53) Fernández-Delgado, N.; Herrera, M.; Pizarro, J.; Galindo, P.; Molina, S. I. HAADF-STEM for the Analysis of Core−Shell Quantum Dots. *J. Mater. Sci.* **2018**, *53*, 15226−15236.
(54) Pizarro, J.; Galindo, P. L.; Guerrero, E.; Yáñez, A.; Guerrero, M. P.; Rosenauer, A.; Sales, D. L.; Molina, S. I. Simulation of High Angle Annular Dark Field Scanning Transmission Electron Microscopy Images of Large Nanostructures. *Appl. Phys. Lett.* **2008**, *93* (15), 153107.
(55) Di, Z.; Chu, P. K.; Zhang, M.; Liu, W.; Song, Z.; Lin, C. Germanium Movement Mechanism in SiGe-on-Insulator Fabricated by Modified Ge Condensation. *J. Appl. Phys.* **2005**, *97* (6), 064504.
(56) Batson, P. E. Silicon $L_{2,3}$ near-Edge Fine Structure in Confined Volumes. *Ultramicroscopy* **1993**, *50*, 1−12.
(57) Euaruksakul, C.; Li, Z. W.; Zheng, F.; Himpsel, F. J.; Ritz, C. S.; Tanto, B.; Savage, D. E.; Liu, X. S.; Lagally, M. G. Influence of Strain on the Conduction Band Structure of Strained Silicon Nanomembranes. *Phys. Rev. Lett.* **2008**, *101* (14), 147403.
(58) Morar, J. F.; Batson, P. E.; Tersoff, J. Heterojunction Band Lineups in Si-Ge Alloys Using Spatially Resolved Electron-Energy-Loss-Spectroscopy. *Phys. Rev. B: Condens. Matter Mater. Phys.* **1993**, *47* (7), 4107−4110.
(59) Fischetti, M. V.; Laux, S. E. Band Structure, Deformation Potentials, and Carrier Mobility in Strained Si, Ge, and SiGe Alloys. *J. Appl. Phys.* **1996**, *80* (4), 2234−2252.
(60) Hybertsen, M. S. Absorption and Emission of Light in Nanoscale Silicon Structures. *Phys. Rev. Lett.* **1994**, *72* (10), 1514−1517.
(61) Kovalev, D.; Heckler, H.; Ben-Chorin, M.; Polisski, G.; Schwartzkopff, M.; Koch, F. Breakdown of the K-Conservation Rule in Si Nanocrystals. *Phys. Rev. Lett.* **1998**, *81* (13), 2803−2806.
(62) Austing, D. G.; Honda, T.; Tarucha, S. A New Design for Submicron Double-Barrier Resonant Tunnelling Transistors. *Semicond. Sci. Technol.* **1996**, *11*, 388−391.
(63) Goldberger, J.; Hochbaum, A. I.; Fan, R.; Yang, P. Silicon Vertically Integrated Nanowire Field Effect Transistors. *Nano Lett.* **2006**, *6* (5), 973−977.
(64) Chen, L.; Cai, F.; Otuonye, U.; Lu, W. D. Vertical Ge/Si Core/Shell Nanowire Junctionless Transistor. *Nano Lett.* **2016**, *16*, 420−426.

https://doi.org/10.1021/acs.nanolett.1c01670
Nano Lett. 2021, 21, 7905−7912